Recent Techniques in Surface Metrology

D. G. A. Ibrahim

Engineering and Surface Metrology Lab., National Institute of Standards, El Giza, Egypt.

Corresponding author email: dahi.abdelsalam@nis.sci.eg

Received on: 10 June 2021; Accepted on: 7 July 2021

Abstract

An overview of the recent techniques used in surface metrology is presented. The techniques used in surface metrology can be classified into two: the first is contact measuring systems and the other is non-contact measuring systems. We start with explanation of the contact and non-contact measuring systems with their merits and demerits in surface metrology. Since the non-contact measuring systems have many advantages in surface metrology, so we proceed by focusing on the non-contact measuring systems and their recent technology. Then we proceed with explanation of the most common methods attached with the non-contact measuring systems used to extract the surface of the object being measured in three dimensional (3D). Recent techniques such as a rotating diffuser and convolution of Chebyshev type 2 and elliptic filters, proposed by the author, are explained in detail to enhance the measurement in surface metrology. Finally, we present some of potential applications in surface metrology such as measurement of steep smooth surfaces, rough surfaces, and opaque surfaces. The selected applications illustrate the major merits of using the non-contact measuring systems: it is possible to measure a relatively large field of view with high precision and in real-time. We end with an overview about estimation of the uncertainty budget in non-contact measuring systems.

Keywords: Surface metrology; Interferometry; Phase unwrapping; Terahertz technology; Phase shifting.

1. Introduction

Surface metrology has many applications in engineering, medicine, and science [1-3]. There are two common measuring systems available for extraction of the object being measured: contact (tactile) and non-contact (non-tactile) measuring systems. Contact or tactile measuring systems are still very common and in many cases meet the requirements of industry in term of accuracy [4]. However, due to the pointwise contact recording, a complete surface measurement is in most cases not possible. Moreover, these measuring systems require direct contact with the surface being measured, which are sometimes not convenient, for example in biological and soft samples [5]. Moreover, the contact measuring systems is considered costly, slow, unsafe, and non-compact. Non-contact or non-tactile measuring systems can

overcome these restrictions. They are non-contact i.e. don't require contact probes with the surface being measured, so it is considered safer. Moreover, they are quite faster and cheaper in comparison with the contact measuring systems. The area of measurement by the non-contact measuring systems is considered wide and various, ranging from research laboratories to industrial production lines. Moreover, it is used intensively nowadays in the field of medicine due to its merits in terms of contrast and non-destructiveness [6]. Non-contact measuring systems can be utilized to extract the phase map of smooth objects easily. However, rough surfaces usually destroy the phase through scattering and multiple reflections, which is observable as speckle effect under coherent lighting [7-8]. A rotating diffuser and convolution of Chebyshev type 2 and elliptic filters are introduced by the author to reduce the speckle noise. The non-contact measuring systems are commonly called optical systems or interferometry. An interferometer is a device that generate the interference pattern or interferogram. It is classified into two types: common-path and non-common path. The interferogram is obtained from interference of two signals: one signal comes from the reference mirror and the other comes from the object being measured. The interferogram captured by a CCD or CMOS camera is called modulated interferogram. The modulated interferogram is demodulated to extract the phase map of the object being measured. Once the phase map is obtained, the height map of the object being measured is extracted via phase-height conversion equation or via fitting algorithms. There are three common methods used for interferogram demodulation. The first is the Fourier transform method [9], the second is the wavelet transform method [10-13], and the third is the phase shifting method [14]. The Fourier transform method can be used to obtain the frequency information of an image. However, it does not tell us the right locations of these frequency components existing in the modulated interferogram. Therefore, the Fourier transform method is useful for analysis of stationary signals (*i.e.* signals whose frequency do not change with position). Modulated interferograms are commonly non-stationary signals, which have different characteristics at different positions in the modulated interferogram. To analyze the modulated interferogram, both spatial and frequency information should be known. The Fourier transform is the most popular algorithm used for interferogram demodulation, but it has poor ability to localize the frequency components of a signal with respect to position and hence provides results with large error [15]. Therefore, another type of transform is modified, namely, Windowed-Fourier Transform (WFT) [16-18]. This version is used for demodulation to provide time-frequency representation with better signal localization. The WFT is based on division of the non-stationary signal into small portions, which are assumed to be stationary. This is done using a window function of a selected width, which is shifted and multiplied with the signal to obtain the small stationary signals. The Fourier transform is then applied to each of these portions to obtain the required transform of the signal. This WFT method uses a fixed window length and therefore gives a fixed resolution at all times. The wavelet transform method improves the fixed resolution in the WFT method to some extent. Moreover, it is a suitable method for demodulation of non-stationary signals and works well with noisy interferograms with no necessity for choice of window in the transform plane [19]. The aforementioned merits of the wavelet transform make it possible to explore the steep-abrupt samples, which have a

sudden variation. The phase shifting technique requires at least three temporal images of a given interferogram, with a step phase offset between the images. The obtained phase is a wrapped phase distribution. This method can deal with object discontinuity. There are many algorithms exist for the phase shifting such as the three-frame, four-frame, five-frame methods. However, the most common phase shifting technique is the four-frame method [14]. The step phase offset between the images can be implemented either by using piezo electric transducer (PZT) or by polarization. Due to the non-linearity of PZT, the polarization method is commonly used the last decades, to generate the step phase offset. Recently, a spatial light modulator (SLM) is used to generate the step phase offset in all directions without moving parts. The merit of using the SLM is that no moving parts used in to generate the step phase offset. This means that the error due to vibration is reduced significantly. Moreover, the shift can be performed automatically in all directions, which in turn increases the spatial frequency and hence increases the resolution of measurement.

2. Measuring systems in surface metrology

As we mentioned in section 1, there are two common methods used in surface metrology. The first is the contact measuring systems and the other is the non-contact measuring systems.

2.1. Contact measuring systems

Contact measuring systems can be classified into two types: contact measuring systems without probes and contact measuring systems with probes. The contact measuring systems without probes are used to measure the thicknesses, openings, depths, etc. of solid samples with moderate accuracy. Examples of contact measuring systems without probes are micrometers and calibers. Contact measuring systems with probes are used commonly to investigate points on large surfaces, parallelism, openings, etc. with reasonable accuracy. Examples of contact measuring systems are, coordinate measuring machine (CMM) [4] and atomic force microscope (AFM) [20]. Measurements by contact measuring systems without probes are performed by inserting the solid sample in between the two jaws of the measuring system. The value of measurement is then appearing in digits at a display unit in case of digital measuring systems. Measurements by contact measuring systems with probes are performed point by point on the surface of the object being measured. The sample is positioned tightly on a flat surface and the probe scans over it point by point. The data of the points are recorded and stored in the machine. The software attached in the machine is used to extract information of the surface being measured. The accuracy of the contact measuring systems is affected by many factors such as the diameter of the probe and temperature. This means that the probe should be calibrated from time to time to ensure better measurement. Contact measuring systems with probes such as CMMs and AFMs are considered costly and slow. This means they are not suitable for real-time monitoring. Moreover, the probe can make scratches of the solid surface and hence it cannot be used to measure soft samples such as polymers and thin films. Also, the contact measuring systems with probes are not compact, which means that it is difficult in some cases to convert them to portable devices to be used outside the Lab. Recently, some types of AFMs for example are manufactured to be portable

devices with medium sizes. The aforementioned drawbacks of the contact measuring systems make us focus on alternative measuring systems, which are the non-contact measuring systems. The merits of the non-contact measuring systems are: cheaper, safer, accurate and compact. The compactness of such devices allows them to be portable devices to be used easily in testing and calibrating the objects onsite.

2.2 Non-contact measuring systems

Non-contact measuring systems use electromagnetic light waves to illuminate the sample, so it is called physically non-contact. The measuring device used in this case is called interferometer. Interferometer is a device that is commonly used to produce fringes from the interference of two signals. Interferometers are classified into two: common-path interferometers and non-common-path interferometers. The main difference between common-path and non-common path interferometers is that the reference beam and object beam travel and reflect nearly in the same time in common-path interferometers, while they are not in the non-common path interferometers. This merit makes the common-path interferometers stable and not subject to vibration. Note that vibration leads to produce noise in the captured modulated interferogram and hence an error arises in measurement. Common-path interferometers are usually designed from one arm architecture, while the non-common path interferometers are usually designed from two arms: one arm directs the beam to the reference mirror, while the other arm directs the beam to the object being measured. Young's interferometer, Michelson's interferometer, Mach-Zehnder's interferometer are examples of non-common-path interferometers [1]. Lateral shearing interferometer (LSI) [6], Zernike's phase contrast interferometer [21], and quantitative differential interference contrast (qDIC) interferometer [22] are examples of common-path interferometers. The lateral shearing interferometer provides a field-of-view of approximately 165µm x 135µm, and the theoretical resolution of 0.6µm by the Rayleigh criterion and temporal stability as 0.76nm. Note that, the Fizeau interferometer is classified as near-common-path interferometer due to the fact that the reflected beams from the reference and the object are not exactly travel in the same time.

2.3. Non-common-path non-contact measuring systems

As we mentioned in section 2, Young's interferometer, Michelson's interferometer, and Mach-Zehnder's interferometer are the common examples of non-common-path interferometers. Michelson interferometers consist of a light source which is divided into two copies by a non-polarizing beam splitter. One copy travels to a reference mirror and the other copy travels to the object being measured. The reflected beams from the reference mirror and the object being measured are combined at the non-polarizing beam splitter to produce interference fringes. These fringes are captured by a CCD camera via an imaging lens placed in front of the CCD camera. Mach-Zehnder's interferometers consist of a light source, beam expander, two mirrors (M), two non-polarized beam-splitters (NPBS), some lenses, and a CCD or CMOS camera. It could be said that, almost of the non-common-path non-contact interferometers consist of two arms; one employs as a reference and the other employs as an object, so these kinds of interferometers are called non-common-path

interferometers, because only two beams are combined. Recently, Abdelsalam proposed a new version of high stable non-common-path interferometer [23]. The proposed snapshot imaging interferometer based on a one-piece polarizing Michelson interferometric scheme, as depicted in Figure 1(a). The proposed interferometer does not require moving parts as in the Thorlabs polarimeter. It consists of three parts; collimating optics with a laser source and a linear polarizer fixed at 45^{o}, a one-piece polarizing interferometer, and a sensing module including a linear polarizer with a rotation angle of 45^{o}. A laser diode beam is used as a light source and collimated with a lens of a focal length of 75mm. The collimated beam with a diameter of around 15mm transmits through a linear polarizer fixed at a rotation angle of 45^{o}. After passing through the measured transmissive object, it passes through the one-piece polarizing Michelson interferometer, which includes a polarizing beam splitter with two optical flat mirrors. The polarizing Michelson interferometer is designed to be a one-piece to avoid vibration. Here, the optical path difference between the two arms of the one-piece polarizing Michelson interferometer is fixed to be in the range of 30µm to 50µm to create a path difference and generate interference fringes. Note that the optical path difference in the one-piece polarizing Michelson interferometer is fixed tightly with stainless steel bars. The stability of the proposed interferometer is in the range of 0.02 degrees, which is around 1nm or less. The collimated beam passes through a non-polarizing beam splitter, then through a polarizing beam splitter to divide the beam into two states: one is P and the other is S. The reflected states pass through the polarized beam splitter and then reflected from the non-polarizing beam-splitter to the linear polarizer to convert one component to the other i.e. from P to S or from S to P. The transmitted states from the linear polarizer is PP i.e. same components. The components are interfered and then recorded by a CCD or CMOS camera. The camera used here is a monochrome camera with a resolution of 2160 x 2560 with pixel size of 6.5µm×6.5µm.

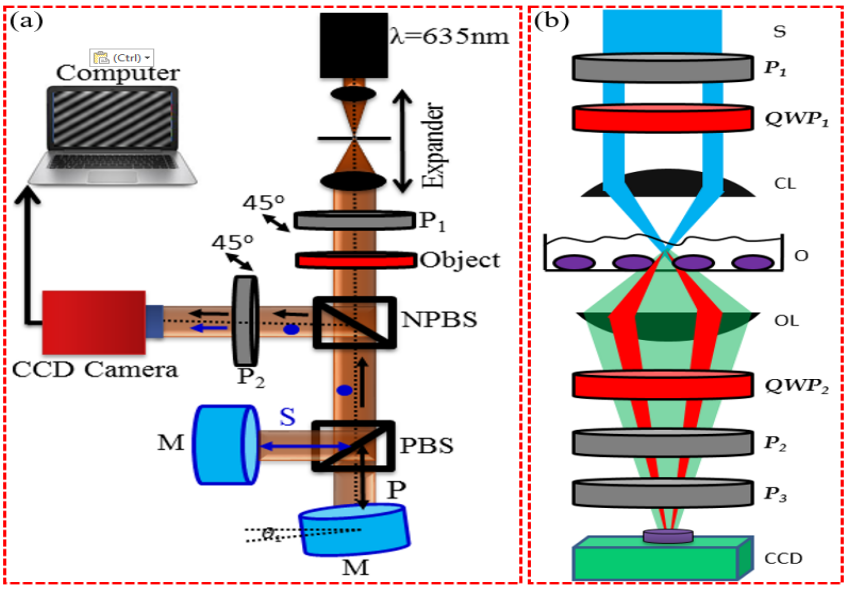

Fig. 1. (a) Schematic diagram of the novel non-common path optical interferometric system. (b) Schematic diagram of the modified common path optical interferometric system.

Figure 2(a) shows a modulated interferogram captured using Figure 1(a) in the absence of the object. Figure 2(b) shows the extracted phase map of Figure 2(a).

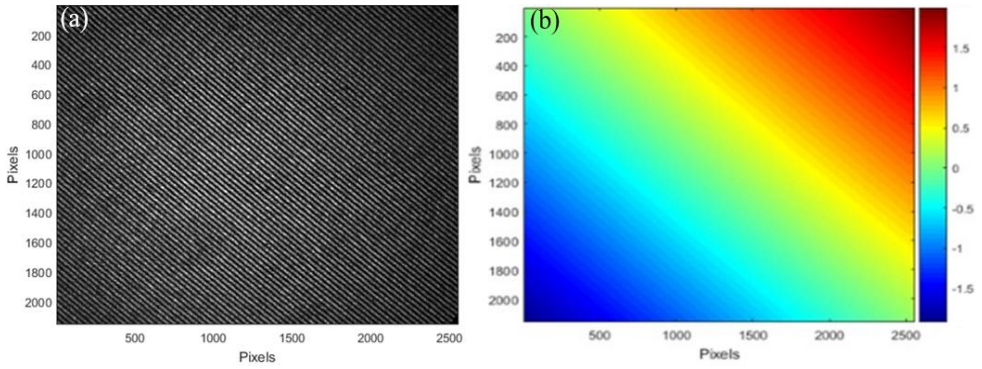

Fig. 2. (a) Produced fringes from Fig. 1(a). (b) Unwrapped phase map of (a) by Itoh algorithm.

The device can be used in many applications such as industry, health, criminal detection, etc. In industry, for example, the novel interferometer can be used to measure the polarimeteric parameters of quarter wave plates, polarizers, liquid crystals, etc., with high precision and within tens of microseconds. Because the novel interferometer is compact (a size of hand grip), it can be used as a portable device and can be used in a crime place. The Merits of using this devise are: simple, compact, and can extract the 3D phase of the sample within tens of milliseconds. The proposed device doesn't have any mechanical rotations. This makes our proposed system a very fast and can extract the polarimetric parameters within tens of milliseconds. Also, the proposed device can extract information data at two dimensional not like the available commercial devices. The intensity of the interferogram in the absence and in the presence of the object being measured are given as:

$$I(-45) = |E_p|^2 + |E_s|^2 + 2\gamma |E_p||E_s| \cos(\phi(-45)),$$
$$I(\theta) = |E_p|^2 + |E_s|^2 + 2\gamma |E_p||E_s| \cos(\phi(\theta)). \quad (2.1)$$

Where $\phi(-45^o)=2k[z_p-z_s]$, and $\phi(\theta^o)=2k[z_p-z_s]+(\delta_p - \delta_s)$ with k is the wavevector given as $k = 2\pi/\lambda$, z_p-z_s is the distance difference between the components P and S from the mirrors to the PBS. The phase of the object is expressd as:

$$\Delta(\theta) = (\Phi(\theta) - \Phi(-45)) = (\delta_p(x,y) - \delta_s(x,y)). \quad (2.2)$$

The phase map extracted by Eq. (2.2) is then converted to height map as:

$$h = \frac{\lambda}{4\pi} \Delta(\theta). \quad (2.3)$$

The 1D profile can be plotted at any two points in the height map to calculate the height of the object being measured at any region in the map.

2.4. Common-path non-contact measuring systems

As we mentioned in section 2, Lateral shearing interferometer (LSI) [6], Zernike's phase contrast interferometer [21], and quantitative differential interference contrast (qDIC) interferometer [22] are examples of common-path interferometers. The idea of the common-path interferometers is based on the fact that the beams travel and reflect

in the same path at the same time. The interferometer in [6] provides a simple experiment and a highly stable configuration. The interferometer consists of a laser source, three axes translation stage to adjust the sample, a microscope objective, a shear plate, and a CMOS or CCD camera. The beam emitted from the laser source passes through the sample and is magnified by the objective lens. The magnified beam falls upon the shear plate at an incidence angle of 45^o. The light incident on the shear plate is reflected from both the front and back surfaces of the shear plate to produce two laterally sheared copies of the beam. The generated lateral beams are self-interfere and the produced interference fringes are recorded by the sensor. In Fizeau interferometer, the reference and the object being measured are in the same path, however, the reflected beams from the surfaces of both the reference and the object being measured are not identical. The reference and the object in this case should be very close in order to obtain identical reflected beams, so such interferometers are called near-common-path interferometry. Figure 1(b) shows a schematic diagram of the modified version of the Zernike's phase contrast interferometer. This version is modified and published by the author in Ref. [24]. The system consists of a laser source (S), a beam expander, three polarizers (P_1 (45^o), P_2 @ 45^o, 135^o, P_3 (45^o)), two QWPs, and a CCD camera. The light from the laser source is expanded by the beam expander and then linearly polarized by a polarizer P_1 fixed at an azimuth angle θ = 45°. The linear polarized light passes through a QWP_1 set at an azimuth angle θ = -45° to the object (O). The two components of the transmitted wave field propagate to interfere at the image plane. The first component proceeds with no deviations, while the second component is modulated. The two components are in fact coherent because all the light comes from a single point source. Note that the Stokes parameter S_2 is simply provided, however, the Stokes parameter S_3 is calculated by adding additional QWP_2. To extract the 3D phase of the object (Δ_{Obj}), we first extract the reference phase (Δ_{Ref}) in the absence of the object and then subtract it from the total phase (Δ_T) in the presence of the object. Here, the total phase (Δ_T) includes the phases of both the reference and the object. Note that the condenser lens (CL) and the objective lens (OL) are used to magnify the tiny objects. First, the reference phase (Δ_{Ref}) in the absence of the object is calculated. Then the object being tested is inserted in the optical system and the total phase (Δ_T) is calculated. From the difference between the total phase (Δ_T) and the reference phase (Δ_{Ref}), the object phase (Δ_{Obj}) is calculated. Here, the phase of the reference is calculated as $\Delta_{Ref} = \tan^{-1}(-S_{3R}/S_{2R})$, the total phase is calculated as $\Delta_T = \tan^{-1}(-S_{3T}/S_{2T})$, then the phase of the object being tested is calculated as $\Delta_{Obj} = \Delta_T - \Delta_{Ref}$.

3. Interferogram analysis in surface metrology

To extract the 3D surface shape of the object being measured, fringes are projected onto the object's surface. The obtained interferogram is a modulated interferogram. To extract the phase map encoded in this modulated interferogram, the modulated interferogram is demodulated. The Fourier transform technique, the phase shifting technique, and the wavelet transform technique can demodulate the modulated interferogram. Each technique for demodulation has advantages and disadvantages in surface metrology. For example, the wavelet transform technique is more suitable for

the analysis of non-stationary signals rather than stationary signals. A stationary signal is a signal whose frequency contents do not change in time, whereas a non-stationary signal is a signal whose frequency contents do change in time or position. Figures 3(a) and (b) show an example of stationary and non-stationary signals, respectively. The three techniques extract the 3D phase map in the range between $-\pi$ to $+\pi$. Such phase is called wrapped-phase, so unwrapping algorithms are used to extract the 3D continuous phase. Examples of unwrapping algorithms are Itoh algorithm [25], Ghiglia algorithm [26], and Graph cuts algorithm [27]. The relation between unwrapped phase and wrapped phase is defined as: unwrapped phase = wrapped phase $\pm 2n\pi$, where n is an integer account for the number of 2π multiples.

The next sub sections explain in detail the Fourier transform technique, the phase shifting technique, and the wavelet transform technique and present how the 3D surface topography of the object being measured is extracted from the modulated interferogram.

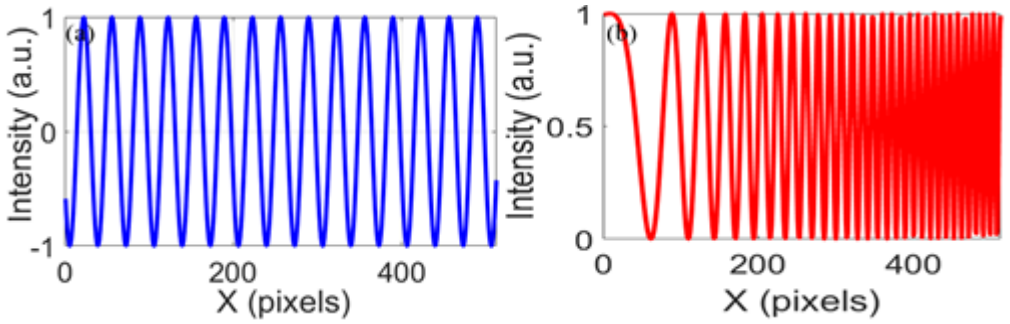

Fig. 3. (a) An example of a stationary signal. (b) An example of a non- stationary signal

3.1. Fourier transform method

The Fourier transform (FT) method is a well-known and popular method for interferogram demodulation. Takeda proposed the Fourier transform method in analyzing the modulated interferogram in 1982 [28]. The intensity of the modulated interferogram parallel to the *y*-axis can be expressed as:

$$g(x,y) = \alpha(x,y) + \beta(x,y)\cos\left(2\pi f_0 x + \phi(x,y)\right) \tag{3.1}$$

where $\alpha(x,y)$, $\beta(x,y)$ are the background illumination and the amplitude modulation of the fringes, respectively, f_o is the spatial carrier frequency, $\phi(x,y)$ is the phase modulation of the interferogram and x, y are axes in x and y, respectively. The expression of Eq. (3.1) can be re-writing as:

$$g(x,y) = \alpha(x,y) + c(x,y)e^{i2\pi f_0 x} + c^*(x,y)e^{-i2\pi f_0 x}, \tag{3.2}$$

where, $c(x,y) = \beta(x,y)e^{i\varphi(x,y)}/2, c^*(x,y) = \beta(x,y)e^{-i\varphi(x,y)}/2$.

The spectrum of the interferogram can be expressed as;

$$G(f,y) = A(f,y) + C(f - f_0, y) + C^*(f + f_0, y). \tag{3.3}$$

where $C(f - f_o, y)$ and $C^*(f + f_o, y)$ are the carrier signals and $A(f, y)$ is DC term. Figure 4(a) shows the 1D profile along the three spectra in frequency domain, and Figure 4(b) shows selected spectrum after centering. A filter window is used to select the carrier signals and shifting that component towards the origin.

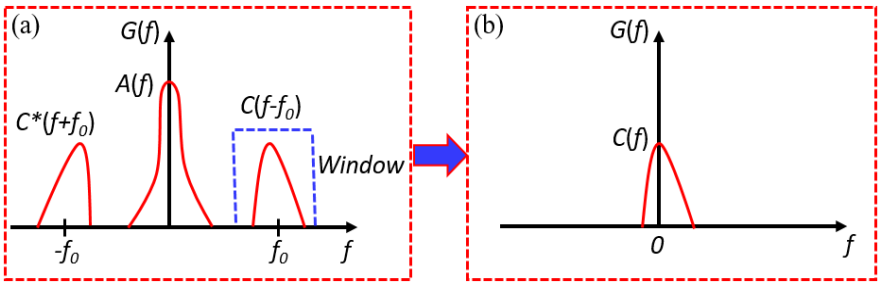

Fig. 4. (a) The spectra in frequency domain of a fringe pattern. (b) The selected frequency component.

The inverse Fourier transform is then applied to the spectrum component $C(f,y)$ to obtain $c(x,y)$. The real and imaginary components of $c(x,y)$ are expressed as:

$$\mathrm{Re}(c(x,y)) = \beta(x,y)\cos(2\pi f_0 x + \phi(x,y)), \tag{3.4}$$

$$\mathrm{Im}(c(x,y)) = \beta(x,y)\sin(2\pi f_0 x + \phi(x,y)). \tag{3.5}$$

The phase is retrieved by dividing (3.5) by (3.4) as:

$$\phi(x,y) = \tan^{-1}\left[\frac{\mathrm{Im}(c(x,y))}{\mathrm{Re}(c(x,y))}\right] = \tan^{-1}\left[\frac{\beta(x,y)\sin(2\pi f_0 x + \phi(x,y))}{\beta(x,y)\cos(2\pi f_0 x + \phi(x,y))}\right] = \tag{3.6}$$

$$\tan^{-1}\left[\tan((2\pi f_0 x + \phi(x,y))\right] = 2\pi f_0 x + \phi(x,y)$$

The obtained phase is limited between $-\pi/2$ and $\pi/2$ due to the arctangent function. The wrapped phase should be unwrapped in order to remove the 2π ambiguity.

The Fourier transform is considered the most popular technique in surface metrology, but it has poor ability to localize the frequency components of a signal with respect to position and hence provides results with large error [15]. Moreover, when the signal is associated with noise, errors would be introduced into the analysis. Therefore, another type of transform is modified to analyze nonstationary signals, namely, Windowed-Fourier Transform (WFT) technique [16-19]. This version is used for interferogram demodulation to provide time-frequency representation with better signal localization. The WFT is based on division of the non-stationary signal into small portions, which are assumed to be stationary. This is done by using a window function of a selected width, which is shifted and multiplied with the signal to obtain the small stationary signals. By introducing the Gaussian window in the spatial domain, WFT can achieve local analysis. The Fourier transform is then applied to each of these portions to obtain the required transform of the signal. This technique uses a fixed window length and therefore has some limitations as it gives a fixed resolution at all times. The WFT of a modulated signal $s(x,y)$ is expressed as [16-19]:

$$WFT(f_x, f_y) = \int_{-\infty}^{+\infty}\int_{-\infty}^{+\infty} s(x,y)r^*(x,y)dxdy, \tag{3.7}$$

where $r(x,y) = \exp[-x^2/2\sigma_x^2 - y^2/2\sigma_y^2]$ is the Gabor transform, which is a Gaussian function and the symbol * denotes the complex conjugate operation. Here the σ_x and σ_y are the standard deviations of the Gaussian function in x and y directions, and selected to be 10, respectively. The Gaussian window is selected

because it has higher emphasis on the data near the window center and lower emphasis on the data further away from the window center. By shifting the central position of the Gaussian window point by point and computing the WFT of the signal, the fundamental spectral component of each local signal can be extracted. Then, by integrating all these spectral components, a universal spectral component can be retrieved as:

$$\int_{-\infty}^{+\infty}\int_{-\infty}^{+\infty} WFT(f_0, f_0)dxdy = F(f_0, f_0). \tag{3.8}$$

Finally, applying the inverse Fourier transform to the universal spectral component, the amplitude and phase can be calculated. This technique uses a fixed window length and therefore has some limitations as it gives a fixed resolution at all times. Wavelet transform (WT) method is used to extract the 3D phase with limiting the large errors in the FT method and extents the resolution in the WFT method.

3.2. Wavelet transform method

The main concept of the wavelet transform is to divide a modulated signal into its various scaled and shifted versions of a mother wavelet. The wavelet transform is a suitable tool for the analysis of non-stationary signals. In this section, the Morlet wavelet transform method is explained to demodulate the interferogram row by row. A row of the modulated interferogram is projected onto the daughter wavelets, which are obtained by both translating and dilating a single basis function, called the mother wavelet. The resulting transformation, which is a two-dimensional complex array, contains the required phase information of that deformed interferogram's row, which can be retrieved by determining the ridge of the transform. A modulus array and phase array can be calculated from the resulting two-dimensional complex array. The direct maximum method can be used to extract the ridge from the modulus array. Several families of mother wavelets are available such as the Haar, Paul, Shannon, Gaussian and Morlet wavelets. The choice of the mother wavelet that will be used must be adapted to the actual information that should be extracted from the signal. The Morlet wavelet provides better localization in both the frequency and spatial domains. The Morlet wavelet is a plane wave modulated by a Gaussian function, and it is expressed as:

$$\psi(x) = \pi^{1/4} e^{i\alpha x} e^{-x^2/2}, \tag{3.9}$$

where $i = \sqrt{-1}$, α is a fixed spatial frequency in the range of 5 to 6 to satisfy the admissibility condition. Daughter wavelets $\psi_{b,a}$ are built by translation on the *x*-axis by *b* (shifting) as a location parameter and by *a* as a dilation parameter (scaling) of the mother wavelet $\psi(x)$ as given by

$$\psi_{b,a}(x) = \frac{1}{a}\psi\left(\frac{x-b}{a}\right). \tag{3.10}$$

A stretched wavelet means large scale wavelet, which has a slow rate of change and hence low frequency. On the other hand, a compressed wavelet means small scale wavelet, which has a rapid change and hence high frequency. The modulated signal $f(x)$ multiplied by scaled, shifted versions of the mother wavelet. The result are

wavelet coefficients that are a function of the scale a and the shifting b and can be expressed as;

$$D(a,b)=\frac{1}{a}\int_{-\infty}^{\infty}\psi^{*}\left(\frac{x-b}{a}\right)f(x)dx, \tag{3.11}$$

where $f(x)$ in our case represents a row of a fringe pattern, * denotes complex conjugation. These coefficients refer to the closeness of the signal $f(x)$ to the wavelet at a particular scale a and translation b. This definition shows that wavelet analysis is a measure of the similarity between the daughter wavelets and the signal itself. The time and frequency localization of the wavelets in the time and frequency domains can be controlled by shifting the wavelet on the time axis and by changing the wavelet scale respectively. The result is two dimensional complex array and it is a function of the scaling parameter a and the shifting parameter b. The modulus and the phase arrays are expressed as:

$$Modulus=|D(a,b)|=\sqrt{[\mathrm{Re}(D(a,b))]^2+[\mathrm{Im}(D(a,b))]^2}, \tag{3.12}$$

$$Phase=\tan^{-1}\left(\frac{\mathrm{Im}(D(a,b))}{\mathrm{Re}(D(a,b))}\right). \tag{3.13}$$

The obtained wrapped phase values are then unwrapped to remove the 2π ambiguity.

3.3. Phase shifting method

In comparison to Fourier transform method, phase shifting method is relatively simple. However, it requires at least three interferograms, with a phase offset between them, in order to extract the phase map of the object being measured. Note that in Fourier transform, only a single interferogram is required to extract the phase map of the object. The phase shifting method is classified into algorithms: the three-frame, four-frame, five-frame algorithms [29]. The most common phase shifting algorithm is the four-frame, which is described in this section as follows. The general equation of intensity of the obtained modulated interferogram can be expressed as;

$$g(x,y)=\alpha(x,y)+\beta(x,y)\cos\left(2\pi f_0 x+\phi(x,y)\right), \tag{3.14}$$

To determine the phase $\phi(x,y)$ of the object being measured, the four frame algorithm was used to extract the phase map of the object. Four images are needed with mutual phase shifts of $\pi/2$ radians between them. The intensity in the four interferograms can be expressed as;

$$g_1(x,y)=\alpha(x,y)+\beta(x,y)\cos\left(2\pi f_0 x+\phi(x,y)\right) \tag{3.15}$$

$$g_2(x,y)=\alpha(x,y)+\beta(x,y)\cos\left(2\pi f_0 x+\phi(x,y)+\pi/2\right) \tag{3.16}$$

$$g_3(x,y)=\alpha(x,y)+\beta(x,y)\cos\left(2\pi f_0 x+\phi(x,y)+\pi\right) \tag{3.17}$$

$$g_4(x,y)=\alpha(x,y)+\beta(x,y)\cos\left(2\pi f_0 x+\phi(x,y)+3\pi/2\right) \tag{3.18}$$

Subtracting (3.17) from (3.15) yields;

$$g_1(x,y)-g_3(x,y)=2\beta(x,y)\cos\left(\phi(x,y)\right) \tag{3.19}$$

Furthermore, subtracting (3.16) from (3.18) gives;

$$g_4(x,y)-g_2(x,y)=2\beta(x,y)\sin\left(\phi(x,y)\right) \tag{3.20}$$

Finally, the required phase is determined by dividing (3.20) by (3.19):

$$\phi(x,y) = \tan^{-1}\left[\frac{g_4(x,y) - g_2(x,y)}{g_1(x,y) - g_3(x,y)}\right]. \tag{3.21}$$

Note that the obtained wrapped phase map is subtracted from $2\pi f_0$ to obtain the phase map of the object being measured. In phase shifting method, the offset phase can be implemented using piezo electric transducer (PZT), however, due to non-linearity of PZT, which produces error in measurement, polarization was proposed as an alternative strategy for offset phase generation. Although this strategy reduces an error in measurement, it hampers its use due to system complexity. Due to the fact that phase shifting requires at least three interferograms, in case of using PZT or polarization, to extract the phase map of the object, so interferograms always attached with noise. This noise causes error in measurement. To reduce this noise, we propose to use spatial light modulator (SLM) for offset phase generation. SLM is a dynamic device that can modulate the amplitude or the phase of the incident light through a 2D matrix structure of discrete pixels. When a slight voltage is applied to the layers of the liquid crystal molecules, a slight rotation in the liquid crystal molecules is produced. The direction of rotation can be clockwise or anti-clockwise. Since there is a relation between rotation angle and phase ($2\pi/\lambda$ (path length)), one can calculate the offset phases θ_j without moving parts.

4. Applications in surface metrology

Quality demands on surface metrology are increasing, especially in the fields of automotive industry, medical technology and semiconductor industry [1]. Here, we focused on three types of surfaces, namely, steep smooth surfaces, rough surfaces, and opaque surfaces. For the steep smooth surfaces, we used the windowed Fourier transform method to enhance the modulated interferogram and the FT method was used to demodulate the modulated interferogram. For the rough surfaces, which is the most challenging, we used the WFT method to enhance the modulated interferogram and the FT method was used to demodulate the modulated interferogram. The convolution of the transfer functions of both Chebyshev type 2 and elliptic filters was used to enhance the roll-off and remove the ripples in pass and stop bands of the object being measured. For the opaque objects, we used the terahertz (THz) radiation combined with a Mach-Zehnder interferometer for 3D extraction of the opaque objects measurement.

4.1. Steep smooth surface measurement

Steep surfaces of step heights need to be measured precisely to be used in many applications such as lithography, semiconductor industry, engineering, and science [1-5]. Coherence scanning interferometer has the capability to measure such surfaces, however, it requires recording a great number of images to extract the 3D surface of the object being measured. Reflectometry works well on reflective surfaces such as mirrors, however, the transmissive surfaces can't be measured by such device. Here, we used a Mach-Zehnder interferometer in combination with FT and WFT methods modified with flat fielding to extract the 3D surfaces of steep heights. The interferometric system has been built up by the author in his Lab at NIS. The programs of FT algorithm, WFT algorithm, and phase shifting algorithm, used for 3D

phase extraction, were written by the author using MATLAB software. The sample being tested is a step height of 1.34μm. We used here single wavelength of 635nm. Figure 5(a) shows the modulated parabolic interferogram. Fig. 5(b) shows correction of (a) with WFT method. The phase map of (a) and (b), reconstructed by the FT method are shown in (c) and (d), respectively. The σ of (a) = 47.11, while the σ of (b) = 10.21. As seen from Fig. 5(d), the coherent noise is reduced significantly by application of the WFT method.

The 1D phase profiles along the red and blue lines of Figures 5(c and d) are shown in Figure 5(e). As seen in Figure 5(e), the slopes of the red and blue profiles are different. The value of δx_1 in the blue profile is around one third of the value of δx_2 in the red profile. This means the roll-off of the blue profile became steeper by around three times in comparison with the red profile. We applied the convolution of the transfer function of Chebyshev type 2 and elliptic filters with the blue profile of Figure 5(e) to obtain steeper roll-off and remove the ripples. Since the convolution is intensity based, so the phase profile is converted to intensity based. We converted the blue phase profile of Figure 5(e) using the formula (10 (1-phase profile/min (phase profile)). The obtained gain is shown in the blue profile of Figure 5(f). The obtained gain of the blue profile of Figure 5(f) is convolved with the transfer function of Chebyshev type 2 and elliptic filters and the result is shown in the black profile of Figure 5(f). As seen in the black profile of Figure 5(f), the roll-off became steeper with no ripples in the bands.

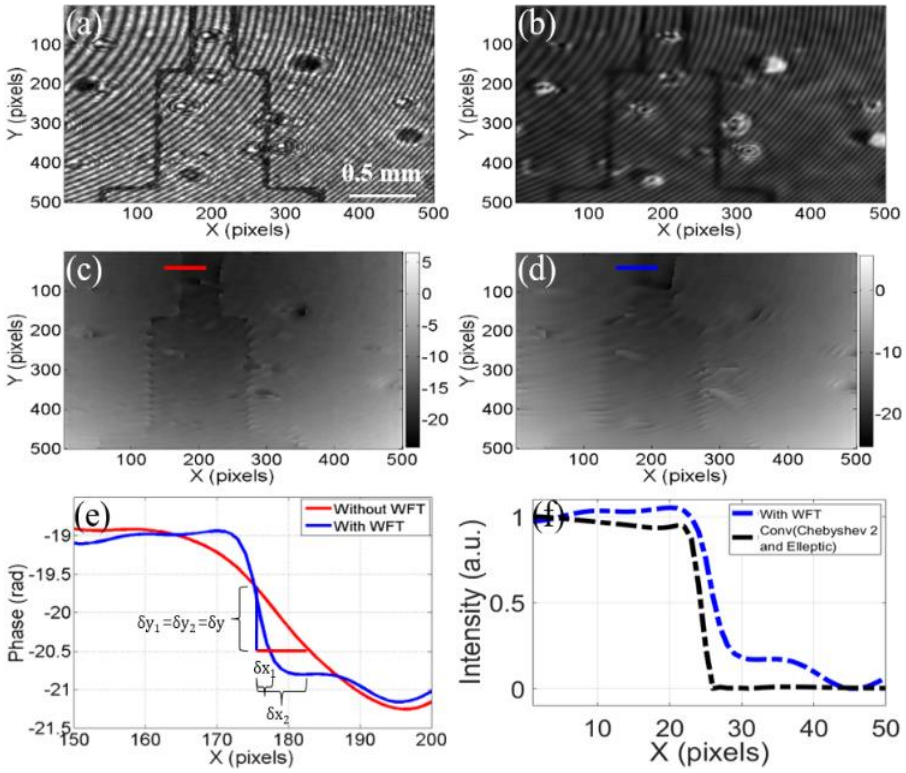

Fig. 5. (a) Modulated interferogram of the second sample. (b) Correction of (a) with the WFT method. (c) phase map of (a). (d) phase map of (b). (e) 1D phase profiles along the red and blue lines of (c) and (d), respectively. (f) Convolution of the blue profile of (e) with the transfer function of Chebyshev type 2 and elliptic filters.

4.2. Rough surface measurement

Almost of surfaces in nature are considered to be rough when investigated by non-contact measuring systems. When polishing is used, rough surfaces turns to smooth surfaces. Since polishing is a complicated process and costs much money, so rough surfaces are common and already available extensively in the application of industry sector. When rough surfaces tested by non-contact measuring systems, the phase values of the rough object are destroyed through scattering and multiple reflections, which is observable as speckle effect under coherent lighting. White light interferometry has been used as low coherence to test the rough objects, but at the expense of bad visibility of the fringes. Here, we proposed to use a rotating diffuser to reduce the speckle noise to some extent. The rest of the noise in the interferogram is reduced further by the WFT method. We then convolved the transfer function of WFT with the transfer function of Chebyshev type 2 and elliptic filters to adjust the roll-off and remove the ripples in the pass and stop bands. The transfer function of Chebyshev type 2 filter for order n may be written as [30]:

$$\left|g_{Ch}(j\omega)\right|^2 = \frac{1}{1+(1/\varepsilon^2 T_n^2(\omega_c/\omega))}, \tag{4.1}$$

where ε is the ripple factor, ω_c is the cut-off frequency, ω is the angular frequency, and T_n is a Chebyshev polynomial of the n^{th} order. The condition of $|g_{Ch}(j\omega)|$ is that it can be zero at some frequencies but cannot be zero over a finite band of frequencies. Also, the real and imaginary parts of $g_{Ch}(j\omega)$ are independent. Chebyshev polynomials of the n^{th} order may be generated recursively by using the relationship [30]:

$$T_{n+1}(\omega) = 2\omega T_n(\omega) - T_{n-1}(\omega), \tag{4.2}$$

along the stop-band, T_n^2 oscillates between 0 and 1, and this causes $|g_{Ch}(j\omega)|$ to oscillate between 0 and $1/(1+1/\varepsilon^2)^{0.5}$. Here, the R_s (values of ripple in the stop band) is selected to be 20dB, while R_p (values of ripple in the pass band) is selected to be 0.5dB. The smaller R_s, the wider is the transition from pass-band to stop-band. We specified a cut-off frequency of 10rad/s and n = 5. Here, the order of the filter has been chosen to be 5 taking into account that the larger n leads to the steeper the roll-off, but large values of n can cause numerical difficulties. The transfer function of the elliptic filter for order n may be written as [30]:

$$\left|g_{ell}(j\omega)\right|^2 = \frac{1}{1+(1/\varepsilon^2 \Gamma_n^2(\alpha, \omega_c/\omega))}, \tag{4.3}$$

where Γ_n is the n^{th} order elliptic rational function and α is the selectivity factor. The amount of ripple in each band is independently adjustable. The ripple factor specifies the pass-band ripple, and a combination of the ripple factor and the selectivity factor specify the stop-band ripple. The cut-off frequency ω_c of this filter is also specified as 10rad/s and n = 5. The elliptic filter has equalized ripples in both the pass-band and the stop-band, providing the fastest roll-off. The convolution of the transfer functions of Chebyshev type 2 and elliptic filters in frequency domain can be written as:

$$G(f_x, f_y) = \left|g_{Ch}(j\omega)\right|^2 \left|g_{ell}(j\omega)\right|^2. \tag{4.4}$$

Using the elliptic filters, a sharp roll-off is obtained at the expense of some small ripples in both pass-and stop-bands. When the convolution is used, the ripples

disappear. We applied the proposed technique on a modulated interferogram of a die recorded experimentally using a Mach-Zehnder interferometer with and without a rotating ground glass diffuser. Here, since the object is rough, so we used a rotating diffuser and a WFT algorithm to suppress the speckle noise in the intensity-contrast image. A 50-mW diode laser with wavelength 635nm coupled into a short-length optical fiber is used as the illumination source. To minimize speckle noise, the spatial coherence of the laser light needs to be mitigated. This is done here by a rotating ground glass diffuser that is placed about 50mm in front of the fiber to scatter and diffuse the light to the back focal plane of a collimating lens placed at a distance of 150mm to collimate the light. The rotating ground glass diffuser is a custom apparatus in which the ground glass is drilled and attached with a screw to a shaft that is connected to a gear assembly and a DC motor with a variable voltage supply. The angular speed of the rotating diffuser is manually adjusted to reduce the contrast of the disturbing speckle pattern to an acceptable level. The collimated light incident on an iris diaphragm adjusted for an opening of about 1.5 cm. The light is then incident on a beam splitter NPBS1 to divide it into two copies with equal intensities. One copy is used as a reference beam and the other as an object beam. The rough object being tested is a cube die. The object beam then illuminates one surface of the die and the light scattered from it is then combined with reference beam at NPBS2 to interfere. The reference and object beams take an approximately equidistant path to the CCD. Some neutral density filters that allow control of the power of the object and reference beams were used prior to the NPBS2. The process of the image acquisition in the CCD camera was carried out with the support of LabVIEW-based software. To reduce the random noise in the recorded interferograms, an average over 50 consecutive captures were recorded. The deformed interferograms were reconstructed using the FT method based Fresnel and the reconstructed intensity-contrast images are shown in Figure 6 (a and b), respectively. The recording and reconstruction distances were found to be 700 mm. In reconstruction, since the object-sensor is large a bit to use the Fresnel transfer function method, so zero padding has been used to avoid aliasing error in the transfer function. The intensity image of a die is enhanced from speckle by using the WFT method as follows. Assume the modulated interferogram intensity is $I(x, y)$. The windowed Fourier transform (WFT) of the modulated interferogram $I(x, y)$ is expressed in frequency domain as:

$$WFT(f_x, f_y) = \int_{-\infty-\infty}^{+\infty+\infty} I(x, y) r^*(x, y) dxdy. \tag{4.5}$$

where $r(x,y) = \exp[-x^2/2\sigma_x^2 - y^2/2\sigma_y^2]$ is the Gabor transform, which is a Gaussian function and the symbol * denotes the complex conjugate operation. Here the σ_x and σ_y are the standard deviations of the Gaussian function in x and y directions, and selected to be 10, respectively. Gaussian window is selected because it has higher emphasis on the data near the window center and lower emphasis on the data further away from the window center. By shifting the central position of the Gaussian window point by point and computing the WFT of the modulated interferogram, the fundamental spectral component of each local signal is obtained. Then, by integrating all the spectral components, a universal spectral component is obtained. The universal spectral component is convolved with $G(f_x, f_y)$ spectrum. Finally, by

applying the inverse Fourier transform to the universal spectral component, the obtained amplitude-contrast image of the object is expressed such that:

$$O(x,y) = WFT^{-1}\{WFT(f_x, f_y) \otimes G(f_x, f_y)\}. \quad (4.6)$$

Where the symbol $\otimes$ stands for convolution. Since the intensity is the amplitude modulus squared, we used the expression of intensity-contrast image after squaring the modulus of amplitude-contrast image. The obtained intensity-contrast image is enhanced from speckle noise as shown in Figures 3 (c and d), before and after using the rotating diffuser, respectively. Figures 6 (a and b) show the amplitude-contrast images without and with the rotating diffuser. Figures 6 (c and d) show the enhanced images of (a) and (b) by the WFT method. The standard deviations of square intensities of (a), (b), (c), and (d) were calculated to be 64.4, 8.6, 33.1, 4.2 decibles (dB), respectively. This means that the proposed technique plays a significant role in speckle noise suppression. Note that the left column images of Figure 6 are without a rotating diffuser, while the right column images are with a rotating diffuser.

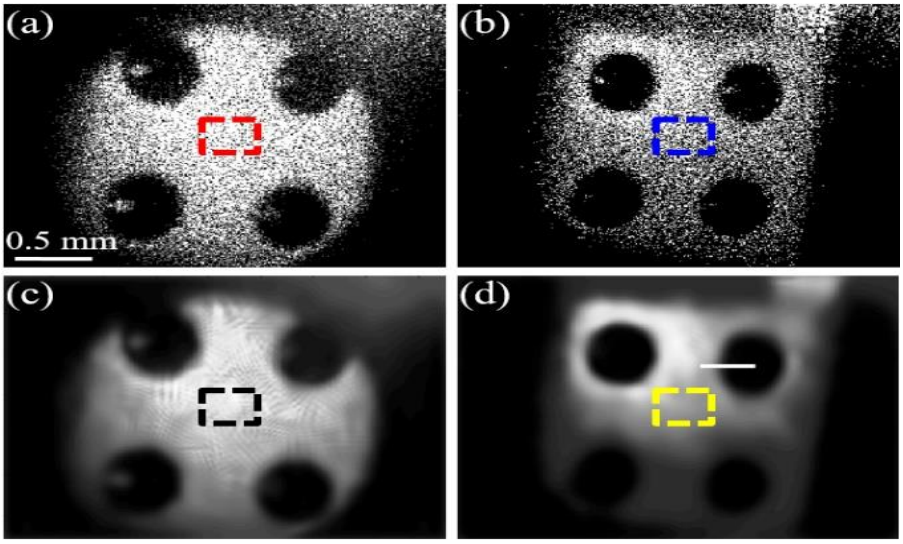

Fig. 6. (a) Intensity-contrast without rotating diffuser. (b) Intensity-contrast with rotating diffuser. (c) WFT of (a). (d) WFT of (b).

4.3. Opaque surfaces measurement

Investigation of opaque objects by visible light (0.4μm to 0.7μm) is not possible. Alternative solution is to use high penetration rays such as terahertz (THz) rays. THz rays range covers the frequencies from 0.1THz to 10THz corresponding to wavelengths of 3mm to 0.03μm between microwave and infrared frequencies in the electromagnetic spectrum [31-33]. Opaque non-metal materials such as ceramics, rubbers, food, plastics can be investigated by THz rays, because THz rays have higher penetration as compared with visible light. There are two available techniques used to visualize the opaque objects. The first technique is point by point time of flight and the second technique is full field THz interferometry. Schematic diagrams to achieve the first and second techniques are shown in Figures 7(a and b), respectively.

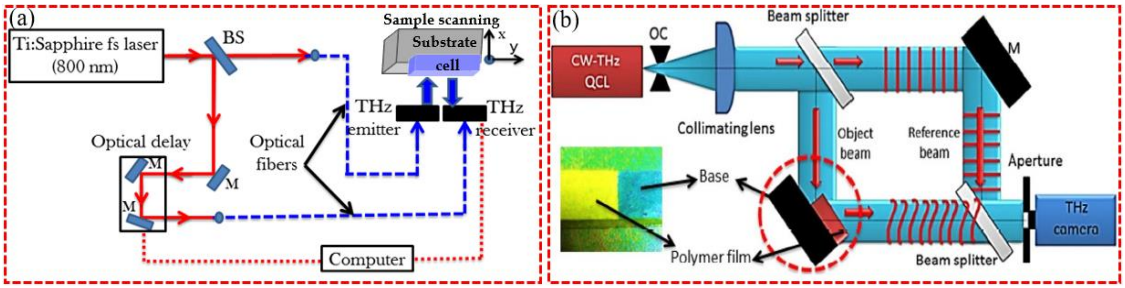

Fig. 7. (a) schematic diagram of Terahertz pulsed imaging (TPI) scanning system with single pixel detector. (b) Schematic diagram of scan-less full field THz interferometer. The wavelength of the quantum cascade laser (QCL) is in the range of 100µm.

The basic idea of the first technique is as follows. When a wave travels from point to point with a distance d between them, it takes a time expressed as: $t_1 = 2\mu d_1/c$, where c is the speed of light. When an object with a thickness h is inserted, then the time $t_2 = 2\mu d_2/c$. From the difference in time, one can easily calculate the thickness h. The basic idea of the second technique is as follows. The opaque sample is inserted in the interferometer and a THz interferogram is captured by THz camera and then analyzed by the FT method, or by the phase shifting method or by the wavelet method. The difference between the first and the second techniques is that the first technique uses a point detector, while the second technique uses a 2D camera. This makes the first technique a time consuming technique because it requires a scanning point by point over the surface of the opaque sample. In the second technique, a single shot THz interferogram is captured in less than a second, so low noise is attached to the THz interferogram. Also, the first technique uses pulsed THz rays, while the second THz technique uses the continuous THz rays. Opaque sample (polymer) of 110µm thickness deposited on steel gauge [5] is tested by the two techniques. Scan over an area of 10mm x 10mm of the sample tested by Fig. 7(a) is shown in Figure 8(a). The profile of one point to extract Δt on the surface is extracted as shown in Figure 8(c). The distance of the sample is then extracted to be 103± 5μm when the index of refraction μ = 1.48. Note that the index of refraction was measured by Terahertz pulsed spectra (TPS) device from Teraview company. The same sample has been tested by Figure 7(b). This was done by capturing the modulated THz interferogram and the analysis was done by FT method. The obtained 3D surface map is shown in Figure 8(b). The height profile along the red line of Figure 8(b) is extracted as shown in Figure 8(d). As seen in Figure 8(b), the thickness of the sample is in the range of 109± 2μm. Note that, the optical chopper (OC) is used in the experiment to do the same job of the rotating diffuser to reduce the speckle noise in the modulated interferogram.

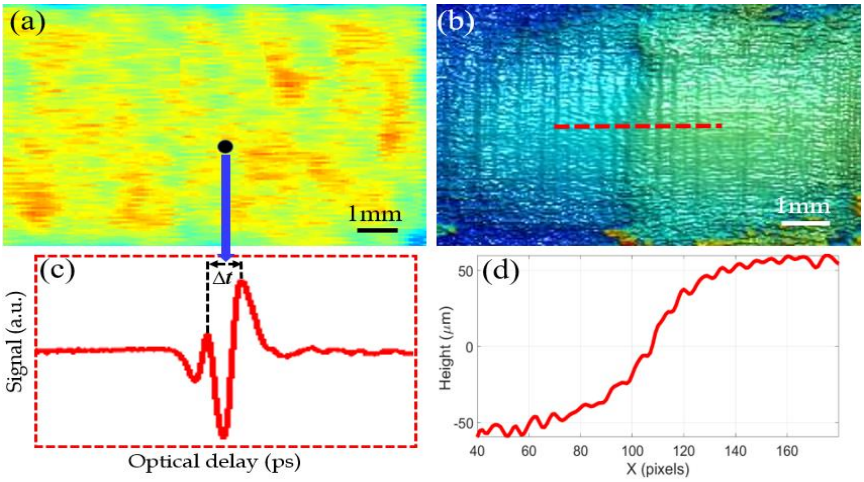

Fig. 8. (a) Photograph of the opaque object. (b) 3D height map of (a) reconstructed by the phase shifting method.

4.4. Estimation of an uncertainty budget in interferometry

In interferometry, the uncertainty budget can be estimated from ten sources [34]. The sources are repeatability, instability of laser light, coherent noise, incomplete parallelism of collimated light, magnification of the microscope objective, Gaussian inhomogeneity of the laser beam intensity, inhomogeneity of surface substrate of the object, chromatic aberration, side lobes effect, and thermal effects. The uncertainty due to coherent noise and chromatic aberrations were calculated to be around 10nm each. The uncertainty due to repeatability and side lobes effect were calculated to be in the range of 5nm each. The uncertainty, due to instability of laser light and due to magnification, were calculated to be in the range of 1nm each. The uncertainty due to incomplete parallelism of the used beam and thermal effect were calculated to be in the range of less than 1nm each. The uncertainty due to inhomogeneity of surface substrate of the object being measured and the Gaussian inhomogeneity of the laser beam were calculated to be in the range of 25nm each. The calculated uncertainty budget from the ten independent sources has been estimated to be in the range of 5% from the object being measured at a level of confidence of approximately 95% for a normal distribution. This value is acceptable in metrology and consistent with that estimated from commercial optical interferometers.

5. Conclusion

We have presented the recent techniques in surface metrology. We conclude that the non-contact measuring systems outperform the contact measuring systems in terms of accuracy, speed, price, safe state, and compactness. Also, the common-path non-contact measuring systems outperforms the non-common-path non-contact measuring systems in term of accuracy and compactness. The Fourier transform method, the wavelet transform method, and the phase shifting method have been explained in detail. The phase shifting method outperforms the Fourier transform method and the wavelet transform in term of speed, while the Fourier transform method outperforms the phase shifting method and the wavelet method in term of speed. The windowed Fourier transform method and the wavelet method are the best

methods in term of noise reduction, while the wavelet transform outperforms the windowed Fourier transform in term of localization and resolution. We also presented the importance of using a rotating diffuser in the experiment to improve the spatial coherence and reduce speckle noise. A novel convolution technique includes the transfer function of Chebyshev type 2 and elliptic filters to enhance the roll-off and remove the ripples in pass and stop bands of the surface has been explained in detail with applications in surface metrology. We demonstrated three potential applications: steep smooth surface, rough surface, and opaque surface. The uncertainty in measurement has been calculated to be in the range of 5% from the length of the object being measured. The modified non-contact measuring systems will be powerful tools for non-destructive inspection of transparent, opaque, and biological samples.

References

1. Ibrahim D.G.A. Optical Metrology with Interferometry, Cambridge Scholars Publishing, London, (2019).
2. M. Quinten M. A practical guide to surface metrology, Springer Nature, Switzerland, (2019).
3. Shichang Du and Lifeng Xi. High definition metrology based surface quality control and applications, Springer Nature, Singapore, (2019).
4. Park J., Kwon K., Cho N. Development of a coordinate measuring machine (CMM) touch probe using a multi-axis force sensor, Meas. Sci. Technol., 17, 2380-2386 (2006).
5. Ibrahim D. G. A., Khalil S., Hamdy H., Eloker M. Multilayer film thickness measurement using ultrafast Terahertz pulsed imaging, J. Phys. Communications,3, 035013, 1-10 (2019).
6. O'connor T., Anand A., Andemariam B., and Javidi B. Deep learning-based cell identification and disease diagnoses using spatio-temporal cellular dynamics in compact digital holographic microscopy, Biomedical Optics Express, Vol. 11, 4491- 4508 (2020).
7. Abdelsalam D. G. Rough surface characterization using off-axis digital holographic microscopy compensated with self-hologram rotation, Current Applied Physics, 18, 1261-1267 (2018).
8. Abdelsalam D., Kim D. Coherent noise suppression in digital holography based on flat fielding with apodized apertures, Optics Express, 19, 17951-17959 (2011).
9. Qian K. Windowed Fringe Pattern Analysis, Chapter 3, Spie press, Bellimgham, Washington, USA, (2013).
10. Gdeisat M. A., Abid A., Burton D. R., Lalor M. J., Lilley F., Moore C., and Qudeisat M. Spatial and temporal carrier fringe pattern demodulation using the one-dimensional continuous wavelet transform: Recent progress, challenges, and suggested developments, Opt. Laser Eng. 47, 1348–1361 (2009).
11. Addison P. S. The Illustrated Wavelet Transform Handbook: Introductory theory and applications in science, engineering, medicine and finance, CRC Press, Taylor & Francis Group, second edition, (2017).

12. Ibrahim D. G. A. Enhancement of the steepness measurement of a film thickness edge using wavelet transforms with fringe thinning, OSA continuum, 3, 1928-1937 (2020).
13. Ibrahim D. G. A. Demodulation of a parabolic interferogram in time domain for rough surface characterization, Applied Physics B: Lasers and Optics, 126:146, 1- 7 (2020).
14. Abdelsalam D. G. Fast phase-shifting technique for 3-D surface micro-topography measurement, Measurement, 135, 106-111 (2019).
15. Zhong J. and Weng J. Spatial carrier-fringe pattern analysis by means of wavelet transform: wavelet transform profilometry, Applied Optics, 43, pp. 4993– 4998 (2004).
16. Qian K. Windowed Fourier transform for fringe pattern analysis, Applied Optics, 43, 2695-2702 (2004).
17. Qian K. Windowed Fourier transform method for demodulation of carrier fringes, Optical Engineering, 43, 1472-1473 (2004).
18. Qian K., Wang H., and Gao W. Windowed Fourier transform for fringe pattern analysis: Theoretical analyses, Applied Optics, 47, 5408-5419 (2008).
19. Rastogi P. and Hack E. Phase estimation in optical interferometry, CRC press, Taylor and Francis group, Boca Raton, London, New York, (2017).
20. Tay A. B. H. and Thong J. T. L. High-resolution nanowire atomic force microscope probe grown by a field-emission induced process, Applied Physics Letters, 84, 5207 (2004).
21. Wang Z., Millet L., Mir M., Ding H., Unarunotai S., Rogers J., Gillette M. U., and Popescu G. Spatial light interference microscopy (SLIM), Opt. Express 19, 1016–1026 (2011).
22. Wen K., Ma Y., Liu M., Li J., Zalevsky Z., and Zheng J. Transmission structured illumination microscopy for quantitative phase and scattering imaging, Front. Phys. 8, 630350-630357 (2021).
23. Ibrahim D. G. A. A series of microscope objective lenses combined with an interferometer for individual nanoparticles detection, Current Applied Physics, 19, 822-828 (2019).
24. Ibrahim D. G. A. Common-path phase-shift microscope based on measurement of the Stokes parameters S_2 and S_3 for 3D phase extraction, Applied Optics, 59, 5779- 5784 (2020).
25. Itoh K. Analysis of the phase-unwrapping algorithm, Applied Optics, 21, 2470-2476 (1982).
26. Ghiglia D., Pritt M. Two-dimensional Phase Unwrapping: Theory, Algorithm, and Software, Wiley, New York, USA (1998).
27. Bioucas-Dias J. M. and Valadão G. Phase unwrapping via graph cuts, IEEE Trans. Image Process, 16, 698-709 (2007).
28. Takeda M., Ina H., and Kobayashi S. Fourier-transform of fringe-pattern analysis for computer-based topography and interferometry, Journal of Optical Society of America, 72, 156-60 (1982).
29. Creath K. Temporal phase measurement methods, chapter 2, Interferogram analysis: digital fringe pattern measurement techniques, Edited by Robinson W.

R. and Reid G. T., Institute of Physics Publishing, Bristol and Philadelphia, pp. 94-140 (1993).
30. Ibrahim D.G.A. Improving the intensity-contrast image of a noisy digital hologram by convolution of Chebyshev type 2 and elliptic filters, Applied Optics, 60, 3823-3829 (2021).
31. Abdelsalam D. G. Steep large film thickness measurement with off-axis terahertz digital holography reconstructed by direct Fourier and Hermite polynomial, Applied Optics, 57, 2533-2538 (2018).
32. Yamagiwa M., Ogawa T., Minamikawa T., Abdelsalam D. G., Okabe K., Tsurumachi N., Mizutani Y., Iwata T., Yamamoto H., and Yasui T. Real-Time Amplitude and Phase Imaging of Optically Opaque Objects by combining of Off-axis Terahertz Digital Holography with Angular Spectrum Reconstruction, Journal of Infrared, Millimeter, and Terahertz Waves, 39, 561-572 (2018).
33. Yamagiwa M., Minamikawa T., Minamiji F., Mizuno T., Tokizane Y., Oe R., Koresawa H., Mizutani Y., Iwata T., Yamamoto H., Yasui T. Visualization of internal structure and internal stress in visibly opaque objects using full-field phase-shifting terahertz digital holography, Optics Express, 27, 33854-33868 (2019).
34. Ibrahim D. G. A. Estimation of an uncertainty budget and performance measurement for a dual-wavelength Twyman-Green interferometer, Journal of Microscopy, 282, 224-238 (2021).